Cite this: *J. Mater. Chem. A*, 2020, **8**, 693

Approaching the Shockley–Queisser limit for fill factors in lead–tin mixed perovskite photovoltaics†

K. D. G. I. Jayawardena,^{†a} R. M. I. Bandara,^{†a} M. Monti,^b E. Butler-Caddle,^b T. Pichler,^c H. Shiozawa,^{†cd} Z. Wang,^e S. Jenatsch,^f S. J. Hinder,^g M. G. Masteghin,^{†a} M. Patel,^h H. M. Thirimanne,^a W. Zhang,^a R. A. Sporea,^a J. Lloyd-Hughes^b and S. R. P. Silva^{†*a}

The performance of all solar cells is dictated by charge recombination. A closer to ideal recombination dynamics results in improved performances, with fill factors approaching the limits based on Shockley–Queisser analysis. It is well known that for emerging solar materials such as perovskites, there are several challenges that need to be overcome to achieve high fill factors, particularly for large area lead–tin mixed perovskite solar cells. Here we demonstrate a strategy towards achieving fill factors above 80% through post-treatment of a lead–tin mixed perovskite absorber with guanidinium bromide for devices with an active area of 0.43 cm². This bromide post-treatment results in a more favorable band alignment at the anode and cathode interfaces, enabling better bipolar extraction. The resulting devices demonstrate an exceptional fill factor of 83%, approaching the Shockley–Queisser limit, resulting in a power conversion efficiency of 14.4% for large area devices.

Received 24th September 2019
Accepted 18th November 2019

DOI: 10.1039/c9ta10543c

rsc.li/materials-a

Introduction

Lead–tin mixed (LTM) perovskites [ABX₃ structure where A is either formamidinium (FA), cesium (Cs), methylammonium (MA) or a mixture of these]^{1,2} are emerging as promising semiconductor systems for photovoltaics (PVs). With bandgaps in the range of ~1.2–1.3 eV,³ close to the optimum Shockley–Queisser bandgap, these devices have demonstrated rapid improvements in performance with single junction cell efficiencies now exceeding 20%.^{4–7} Furthermore, Pb–Sn based systems are also of significant interest as low bandgap cells for all perovskite multi-junction solar cells,^{1,8–10} which expands the potential towards developing an all solution processed PV device architecture with efficiencies exceeding the single

junction efficiency limit. While these LTM perovskite PVs have demonstrated short circuit current densities (J_{sc}) exceeding those of the best performing Pb only perovskite PVs⁵ and respectable open circuit voltage (V_{oc}) losses of ~200 meV,⁵ their fill factors (FFs) are often found to be lagging, with the best achieved values being below 80%.^{11–13} This is in particular due to many non-radiative recombination loss pathways including grain boundary recombination,¹⁴ recombination with defects due to the oxidation of Sn²⁺ to Sn⁴⁺ (ref. 15) and recombination in the charge selective transport layers. For Pb-only perovskite PVs, there is now growing understanding of processing routes such as the incorporation of excess iodide,^{2,16} which has been found to significantly improve device stability and performance. While recent work has indicated bromine incorporation as a possible route towards improving LTM perovskite device characteristics,¹⁷ there is currently a lack of similar understanding of suitable protocols on LTM perovskite absorbers that would enable FFs exceeding 80% to be achieved.

In this work, we outline a route towards improving LTM perovskite PVs based on guanidinium bromide (GABr) treatment, which leads to significant improvements in their optoelectronic properties. Using the triple cation system of Cs_{0.05}FA_{0.79}MA_{0.16}Pb_{0.5}Sn_{0.5}I₃ as the perovskite absorber, we demonstrate that devices based on the inverted architecture of ITO/PEDOT:PSS/LTM perovskite/PCBM/ZnO/BCP/Ag can achieve high FFs approaching 83% and a champion power conversion efficiency (PCE) of 14.4% following the bromide post-treatment. In comparison, an untreated reference device architecture shows a lower PCE of 12.2%. The high FFs obtained

^aAdvanced Technology Institute, Department of Electrical and Electronic Engineering, University of Surrey, Guildford, Surrey, GU2 7XH, UK. E-mail: s.silva@surrey.ac.uk^bDepartment of Physics, University of Warwick, Gibbet Hill Road, CV4 7AL, UK^cFaculty of Physics, University of Vienna, Boltzmannstrasse 5, A-1090 Vienna, Austria^dJ. Heyrovsky Institute of Physical Chemistry, Czech Academy of Sciences, Dolejskova 3, 182 23 Prague 8, Czech Republic^eClarendon Laboratory, Department of Physics, University of Oxford, Parks Road, Oxford OX1 3PU, UK^fFluxim AG, Winterthur, Switzerland^gThe Surface Analysis Laboratory, Faculty of Engineering and Physical Sciences, University of Surrey, Guildford GU2 7XH, UK^hNational Physical Laboratory, Hampton Road, Teddington, Middlesex, TW11 0LW, UK

† Electronic supplementary information (ESI) available. See DOI: 10.1039/c9ta10543c

‡ These authors contributed equally.

are observed to be close to the theoretical limits predicted by the Shockley–Queisser limit (88%). Analysis of the LTM perovskite based on optical, charge transport and ultraviolet photoelectron spectroscopic measurements indicates that the origin of the high fill factors is the modification of the energy level alignment. The quasi Fermi levels of the LTM perovskite absorber and the transport layers maximize charge extraction through the incorporation of Br⁻ into the perovskite lattice. While it may be hypothesised that similar improvements are possible based on other organobromide systems, we note that some of these systems (for example formamidinium bromide) can modify the perovskite composition itself unlike GA⁺ whose cationic radius inhibits its incorporation into the 3D LTM perovskite structure.¹⁸ This does not enable a clear understanding of the impact of the post-processing protocols. As a result, this study focused on utilising GABr only.

Results and discussion

Impact of post-treatment on structural characteristics

The overall LTM perovskite absorber deposition process for the reference and GABr treated samples was carried out based on a combination of the appropriate anti-solvent and thermal annealing, as reported previously by Bandara *et al.*¹⁹ and is depicted in Fig. 1a and b. A representative scanning electron micrograph of a “reference” film prepared using this protocol is given in Fig. 1c while a representative scanning electron micrograph of such a film following this post-treatment process is shown in Fig. 1d. For post-treatment of the above LTM perovskite absorber, we utilized a guanidinium bromide (GABr) solution in 2-propanol at a concentration of 5 mg ml⁻¹ in combination with a thermal treatment that enables the restructuring of the LTM absorber layer followed by an additional 2-propanol wash enabling the removal of unreacted guanidinium cations. The removal of the unreacted guanidinium cations avoids the formation of an insulating surface layer that can negatively impact charge extraction. To identify the impact of the post-treatment on the grain growth process, we carried out a grain size analysis for both the reference and post-treated films. Prior to the post-treatment process, the grains are observed to show a normal distribution with regard to size with an average grain size of 435 ± 33 nm (Fig. 1e). The GABr post-treatment process is observed to result in a more bi-modal distribution (Fig. 1f) with average grain size values of 495 ± 25 nm and 594 ± 14 nm, indicative of an Ostwald ripening process.²⁰ We note that the grain sizes observed herein are in agreement with previously reported values for LTM perovskites.^{4,5}

Following the study of the impact of the GABr post-treatment on the morphology of the LTM perovskite absorber, we evaluated the impact of the GABr post-treatment process on the composition of the LTM perovskite through XPS, ToF-SIMS and EDXS on the thin film surface as well as on the film cross-sections. EDX spectra obtained on the surface of the film indicate the presence of Br⁻ (Fig. S1†) which is also confirmed by XPS analysis (Fig. 2a and S2†). Furthermore, the GABr surface treatment is also observed to result in a change in the local

chemical environment as is evident from the shifts observed for the binding energy of I3d for the GABr treated sample in comparison to that of the reference (Fig. 2a). Following the above, we proceeded to estimate the composition of the perovskite phase closer to the surface of the LTM perovskite absorber. Based on the XPS spectra obtained for the I3d & Br3d signals (Fig. 2a and b), an I⁻ : Br⁻ ratio of 0.8 : 0.2 is estimated for the surface. Based on the above, we tentatively assign a perovskite phase of the form Cs_{0.05}FA_{0.79}MA_{0.16}Pb_{0.5}Sn_{0.5}(I_{0.8}Br_{0.2})₃ (CsFAMAPbSnI_{2.4}Br_{0.6}) for the surface region of the LTM perovskite following the GABr treatment. It is noted that an O1s signature is also observed for the LTM perovskite films (Fig. 2c) which is anticipated due to exposure of samples to the ambient environment during transfer from a glovebox to the XPS system.

In order to identify whether the above-mentioned LTM perovskite of the form CsFAMAPbSnI_{2.4}Br_{0.6} is present throughout the thickness, or a more “graded” type semiconductor with a different I⁻ : Br⁻ to that calculated above is present throughout the thickness of the films, we carried out ToF-SIMS measurements. Analysis of the negatively charged species present in the film (*i.e.* mainly the anions present in the perovskite absorber) (Fig. 2d) indicates a nearly uniform I⁻ content throughout the thickness of the film. Interestingly, the Br⁻ signal is also observed throughout the thickness of the entire perovskite film, indicating that the impact of the post-treatment process in our films is not restricted to the surface and the subsurface region of the LTM perovskite absorber. Based on photoluminescence spectroscopy measurements (as discussed later), this increase in Br⁻/(I⁻ + Br⁻) results in a wider-bandgap perovskite. In addition to the above where the incorporation of Br⁻ is observed throughout the thickness of the film, we note the increased Br⁻ content observed closer to both surfaces of the LTM perovskite absorber. Therefore, it is proposed that following the GABr treatment, an absorber of the form CsFAMAPbSnI_{2.4}Br_{0.6}/CsFAMAPbSnI_{3-x}Br_x/CsFAMAPbSnI_{2.4}Br_{0.6} is formed where 0 < x < 0.6.

Following the evaluation of the Br⁻ distribution through the thickness of the film, we proceeded to examine the distribution of the guanidinium cation through the thickness of the film. The ToF-SIMS characteristics for the positively charged species (Fig. 2e) indicate that the concentration of the guanidinium cations decreases exponentially from the surface on which the GABr treatment is carried out to ~50% of the LTM perovskite absorber thickness followed by a plateauing of the guanidinium cation content at greater depths. This observed decrease in the guanidinium cation content is most likely to be due to the larger ionic radius of this species (278 pm)²¹ as compared to the smaller ionic radius of Br⁻ (196 pm).²² In order to verify the above observations based on ToF-SIMS analysis, we carried out EDXS mapping on the cross-sectional samples of the LTM perovskite absorbers (Fig. 2f). Evaluation of these maps for the Br⁻ distribution indicates the presence of Br⁻ throughout the thickness of the film, in agreement with the observations made from the ToF-SIMS measurements as discussed above. In addition to the above, a bright region is clearly visible closer to the interface of the LTM perovskite and the Pt layer deposited

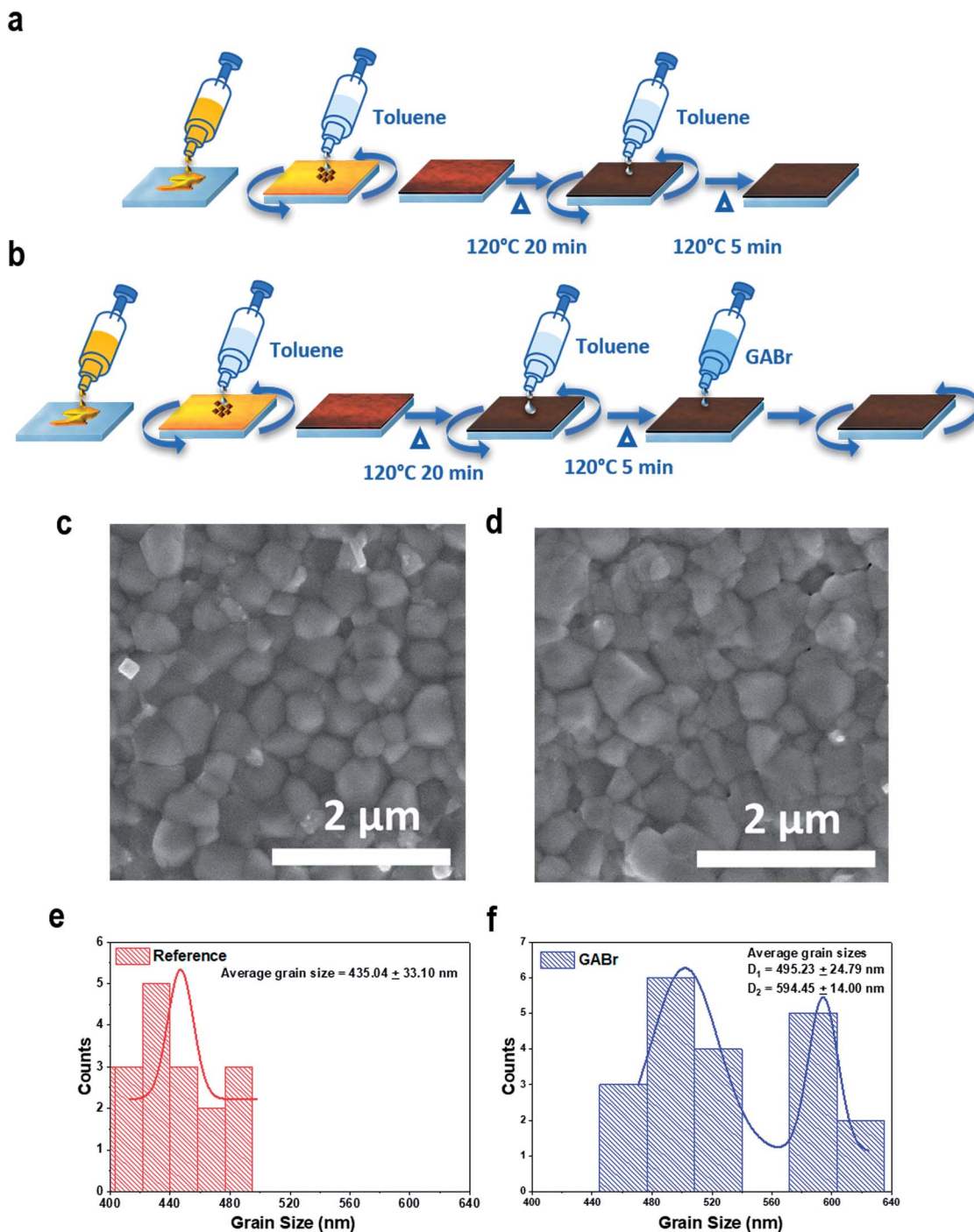


Fig. 1 (a) Schematic depicting the process steps followed for the preparation of the reference and (b) GABr treated LTM perovskite films. (c) SEM micrographs of reference and (d) GABr treated perovskite thin films. The related grain size distribution analysis for (e) reference and (f) GABr treated samples indicates a change in the average grain size from 435 nm to a bi-modal distribution with average grain sizes of 495 nm and 594 nm following GABr treatment.

for the preparation of the cross section. We have observed similar characteristics for lead only perovskite films which have not undergone any post-treatment process (Fig. S3†) which we attribute to a charge build-up due to the formation of a more insulating organic layer on the film surface. However, based on the available evidence, it is not possible to assign this region to

any specific organic species such as the guanidinium cation alone.

Based on ToF-SIMS analysis, it is evident that following the GABr post-treatment, there is a varying concentration of (mainly) guanidinium through the thickness of the film prior to plateauing to a fixed concentration as well as high

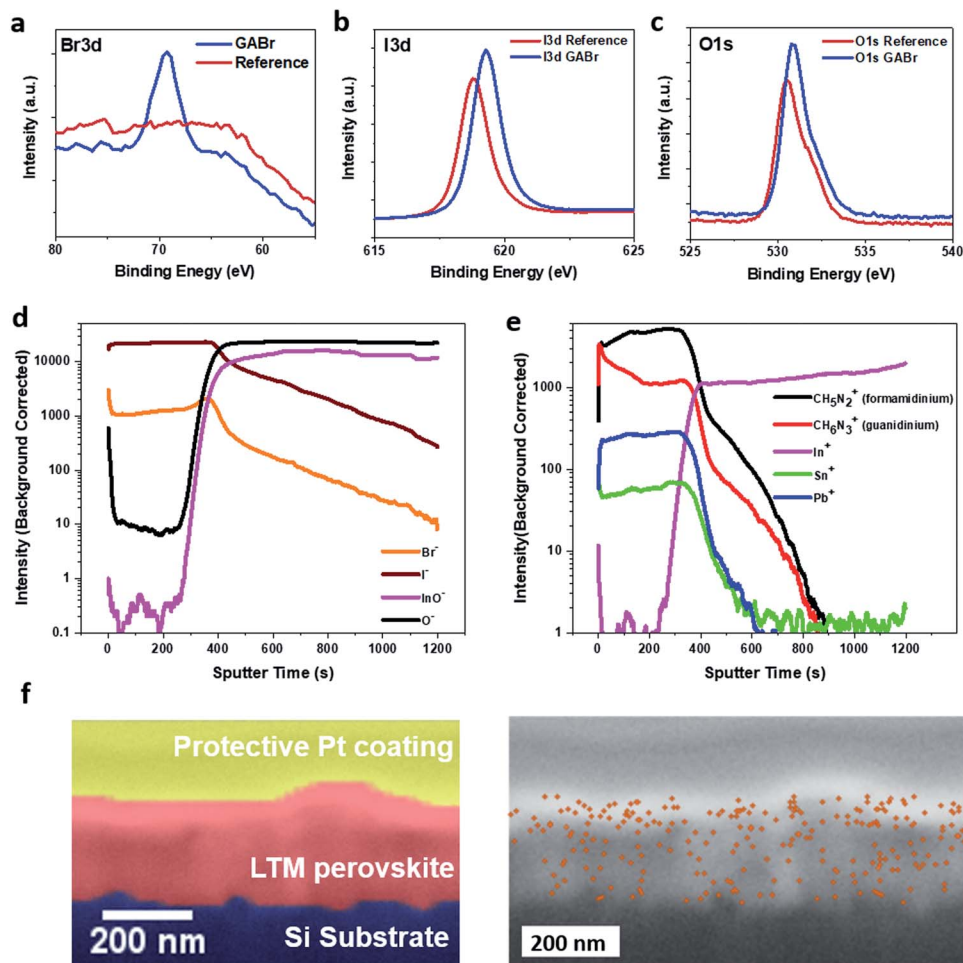


Fig. 2 XPS spectra showing the (a) Br3d peak indicating the incorporation of Br⁻ following the post-treatment process and (b) slight shifts in the I3d peak indicating the change in the local chemical environment. (c) The O1s peak observed for both reference and LTM perovskite samples. The depth profiles obtained through ToF-SIMS for (d) the anions and (e) the cations. The Br⁻ concentration is observed to be slightly higher closer to the two surfaces of the LTM perovskite film while the GA⁺ content is observed to decrease through the thickness prior to achieving a constant “loading”. (f) The EDX mapping of the cross-sectional micrograph of the treated perovskite layer showing Br⁻ distributed throughout the thickness of the film.

concentration of Br⁻ at the two “surfaces” of the film. While guanidinium has been suggested to be too large to form a stable 3D perovskite phase on its own, recent work indicates the possibility of forming a stable 3D perovskite phase based on multi-cation perovskite systems.^{23,24} Furthermore, guanidinium in combination with Sn²⁺ has also been reported to form 2D perovskites.²⁵ Therefore, in order to identify whether a new perovskite phase is formed, we carried out thin film X-ray diffraction (XRD) analysis of both the reference and GABr treated LTM perovskites. The XRD scans for neither the reference nor the GABr treated samples (Fig. S4†) show evidence for the presence of additional lead halide^{26,27} phases typical of triple cation lead only systems. Nor did we observe the presence of any tin halide phases. The lack of any such excess phases in both the reference and the GABr treated samples indicates that the absorber formed is based on the Pb²⁺ in the starting precursor mix while the Sn²⁺ content is based on the un-oxidized content present following the treatment protocols followed here. With

regard to the GABr treatment carried out on the LTM perovskites, there remains the question about whether the guanidinium cation is incorporated into the perovskite lattice. In their recent study, Zhang *et al.* indicated that the incorporation of a moderate level of guanidinium into the perovskite films can result in the formation of either 1D/3D or 1D/2D/3D perovskite systems.^{23,24} However, this has been observed to result in an increase in the perovskite lattice parameters as opposed to the decrease in the lattice parameters observed herein following the GABr treatment. Therefore, it is concluded that the excess guanidinium is segregated either at the grain boundaries or at the surface of the LTM perovskite absorber. Following the confirmation of the absence of the formation of the above perovskite phases, we proceeded to analyze the reduction in lattice parameters (or the shift to higher 2θ) (Fig. 3a) following the GABr treatment. For this purpose, we carried out a modified Williamson–Hall strain analysis^{28,29} for the perovskite absorber (Fig. 3b and c) which indicates an increase in micro-strain

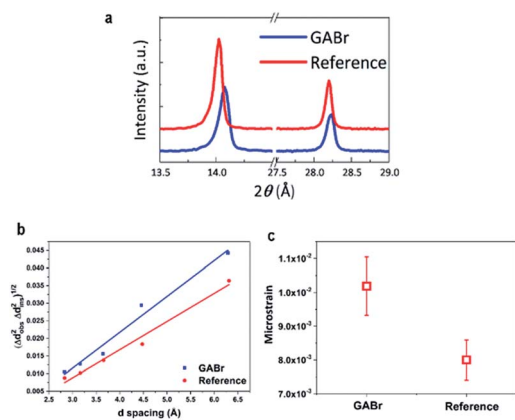


Fig. 3 (a) XRD spectra of the two films (100 and 200 peaks shown here) showing peak shifts with GABr treatment to higher 2θ (lower d -spacing). (b) Fits for strain analysis based on the modified Williamson–Hall method and (c) the micro-strain values calculated for the reference and GABr treated films.

following the GABr treatment process. Such an increase in micro-strain is anticipated mainly due to the concentration gradient observed for the large guanidinium cation which can influence the perovskite grains formed in the direction perpendicular to the film surface.

Impact of post-treatment on optical characteristics

In order to identify the origins of the observed enhancement, we probed the optical and electronic properties of the perovskite absorber layer. For this purpose, steady-state photoluminescence measurements were carried out through illumination from the GABr treated surface (referred to as back excitation) as well as the substrate side (referred to as front

excitation) of the perovskite film (Fig. 4a). Comparison of the front and back excitation spectra obtained for the reference and GABr treated perovskite films (Fig. 4b) indicates a blue shifting of the PL emission following the GABr treatment, indicative of a bandgap increase from ~ 1.25 eV for the reference to ~ 1.30 eV (Fig. S5†) after GABr treatment. This blue shift is in agreement with the Br^- incorporation observed above based on ToF-SIMS measurements and indicates the incorporation of Br^- into the perovskite lattice.³⁰ Further analysis of the films based on the initial photoconductivity in optical-pump THz-probe (OPTP) spectroscopy using methods outlined previously³¹ indicates that the GABr treatment slightly lowers the overall mobility of the absorber layer to $3 \text{ cm}^2 \text{ V}^{-1} \text{ s}^{-1}$ from $11 \text{ cm}^2 \text{ V}^{-1} \text{ s}^{-1}$ for the reference (Fig. 4c). While the increased Br content enhances the momentum scattering due to disorder and/or a change in electron–phonon coupling, thereby lowering the mobility, the inter-band recombination time remains long, at over 5 ns before and after GABr treatment, as estimated from the OPTP dynamics at later delay times, circumventing the non-exponential recombination dynamics evident in the OPTP at early pump–probe delay times (< 1 ns), when bimolecular recombination contributes.³¹ The sufficiently high mobilities and slow recombination yield diffusion lengths of around 490 nm (reference) and 270 nm (GABr treated). We note that these values are lower than those that have been recently reported in the literature based on double A-site cation perovskites,⁶ indicating that further careful optimisation of these triple cation LTM perovskites is required, particularly to increase the light absorption properties. However, the carrier diffusion lengths observed above are compatible with the LTM perovskite absorber thickness of ~ 300 nm as used in photovoltaic devices discussed in the next section which ensures that the carrier diffusion lengths are not the limiting factor for the efficiency of the devices studied herein. In addition to the

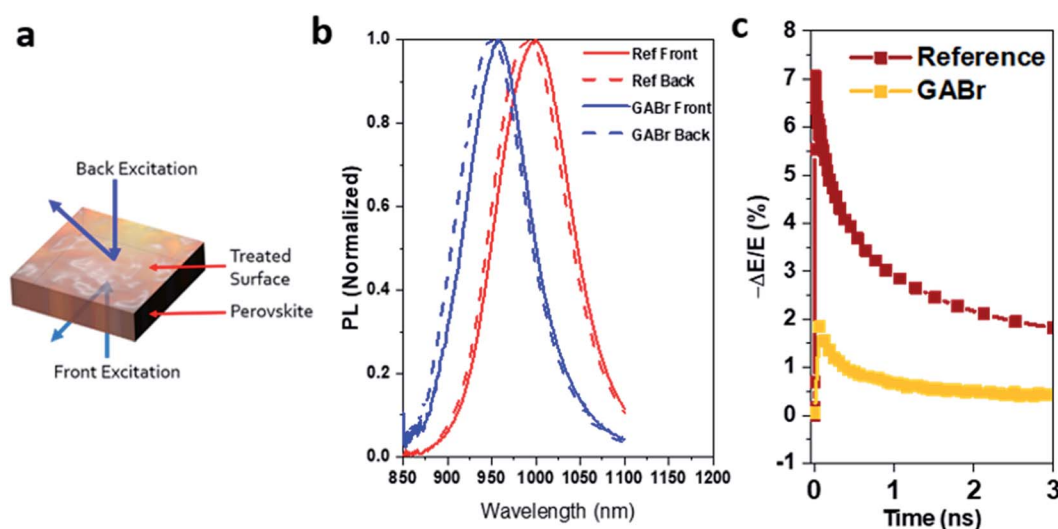


Fig. 4 (a) Schematic representation of the front and back excitation of the surface treated LTM layer where the back excitation is done at the treated surface. (b) Steady state PL spectra obtained from the front and back excitation of the perovskite layer (excitation wavelength = 475 nm), where a blue shift of PL peaks for the GABr treated LTM perovskite is obtained regardless of the surface of excitation. (c) Photoconductivity dynamics from optical-pump THz probe spectroscopy.

carrier mobilities and diffusion length, we also evaluated the carrier lifetimes for both the reference and the GABr treated LTM perovskites based on the optical pump THz probe spectroscopy measurements, which yielded similar lifetime values of ~ 8 ns, indicating that the post-treatment process does not influence the carrier lifetimes. We note that these carrier lifetime values are similar to values previously reported in the literature⁵ for LTM perovskites of similar thicknesses.

Photovoltaic device performance

To identify the impact of the GABr treatment on PV device performance, we fabricated and tested LTM perovskite PVs using the inverted architecture of ITO/PEDOT:PSS/LTM perovskite/PC₆₀BM/ZnO/BCP/Ag (Fig. 5a). We note that we have incorporated a thin layer of ZnO between the PC₆₀BM and BCP layers as it was found to result in lower V_{oc} losses. The current density (J)-voltage (V) behaviours of the best performing reference and GABr treated PVs are shown in Fig. 5b and the distributions of photovoltaic device parameters are given in Fig. 5c-f and Table 1. We observed an improvement in J_{sc} from 23.5 mA cm^{-2} to 24.3 mA cm^{-2} following GABr treatment. The enhancement in the J_{sc} is identified with the improved photocurrent generation throughout the whole wavelength range as evident from External Quantum Efficiency (EQE) measurements (Fig. 5c), indicative of better charge extraction. However, we do note a slight decrease in the V_{oc} from 0.73 V to 0.72 V following the GABr treatment. Most notably, the FF of the device increases from $\sim 70\%$ to values exceeding 80% with the highest value of 83% . Based on a survey of reported work in the literature (Fig. 5h), we note that this, to the best of our knowledge, is the highest reported FF for Sn incorporated perovskite PVs and approaches the best FFs observed for Pb-only perovskite PVs.³² The multiple enhancements achieved for the device parameters following the GABr treatment enable a PCE of 14.4% to be reached as opposed to the 12% obtained for the reference device. Furthermore, tracking of the photocurrent at the maximum power point (Fig. 5b inset) indicates a relatively stable response over time for the GABr treated device in comparison to the stronger decrease over time observed for the reference devices. In order to determine if the GABr post-treatment influences the background carrier density of the LTM perovskite devices, we carried out capacitance-voltage measurements using the Mott-Schottky analysis based on the following relationship:

$$\frac{1}{C^2} = \frac{2}{qA^2\epsilon N} V \quad (1)$$

where C is the capacitance, q is the electronic charge, A is the device area, ϵ is the dielectric constant and N is the carrier density. Based on the fits obtained for the $1/C^2$ vs. V plot (Fig. 5i), we estimate a carrier density of $\sim 2-3 \times 10^{15} \text{ cm}^{-3}$ for both the reference and the GABr treated films, which is suggestive of the fact that the post-treatment process does not lead to a significant alteration in N and therefore the electronic properties of the LTM absorber. Based on the similar carrier lifetimes observed before the optical pump THz probe spectroscopy

measurements and the similar carrier densities from the Mott-Schottky analysis, it is evident that the origin of the improved device fill factors is the improved absorber/contact junctions and interfaces as discussed later.

In addition to the above, studies were also carried out on the impact of the voltage sweep rate on the hysteretic behavior of the reference and GABr treated LTM perovskite devices (Fig. 5j) based on the hysteresis index defined as³³

$$\text{Hysteresis index} = \frac{\text{PCE}_{\text{reverse}} - \text{PCE}_{\text{forward}}}{\text{PCE}_{\text{reverse}}} \quad (2)$$

The analysis indicates a fairly high hysteresis for scan rates below 100 mV s^{-1} which reduces significantly at higher sweep rates. Throughout the whole range of sweep rates studied here, the GABr treatment has resulted in the reduction of the hysteresis index as is evident from the lower hysteresis index calculated for the GABr treated films in comparison to the reference devices. We note recent work on Pb perovskites³⁴ which only consists of iodide as the halide where visible light illumination has been observed to induce variations in strain, which in turn impact the temporal stability of the PV performance. However, the similar behaviour in LTM perovskites is less well understood at present.

Estimation of FF limits

Following the observations made on the high device FF for the LTM perovskite system utilized in this work, we estimated the theoretical limits for the FF of the Pb-Sn perovskites based on the empirical expressions developed by Martin Green³⁵ for a solar cell whose output current (I)-voltage (V) relationship is given by

$$I = I_L - I_0 \left\{ \exp \left[\frac{q(V + IR_s)}{nkT} \right] - 1 \right\} - \frac{V + IR_s}{R_{sh}} \quad (3)$$

where I_L is the photocurrent, I_0 is the diode saturation current, R_s and R_{sh} are the series and shunt resistances (respectively), n is the diode ideality factor, k is the Boltzmann constant and T is the cell temperature. The normalized values for the open circuit voltage (v_{oc}) can be defined as

$$v_{oc} = V_{oc} \frac{q}{nkT} \quad (4)$$

The limiting cases when R_s is negligible and R_{sh} is large result in the empirical relationship for the maximum fill factor as

$$\text{FF}_0 = \frac{v_{oc} - \ln(v_{oc} + 0.72)}{v_{oc} + 1} \quad (5)$$

The dependency of FF_0 values on the bandgap and different diode ideality factors is given in Fig. 6a where the upper limit for V_{oc} has been estimated based on a thermodynamic loss of 300 mV . Considering an ideal V_{oc} of 1 V based on the bandgap of the GABr treated LTM perovskite absorber (1.30 eV) and assuming that recombination within the semiconductor takes

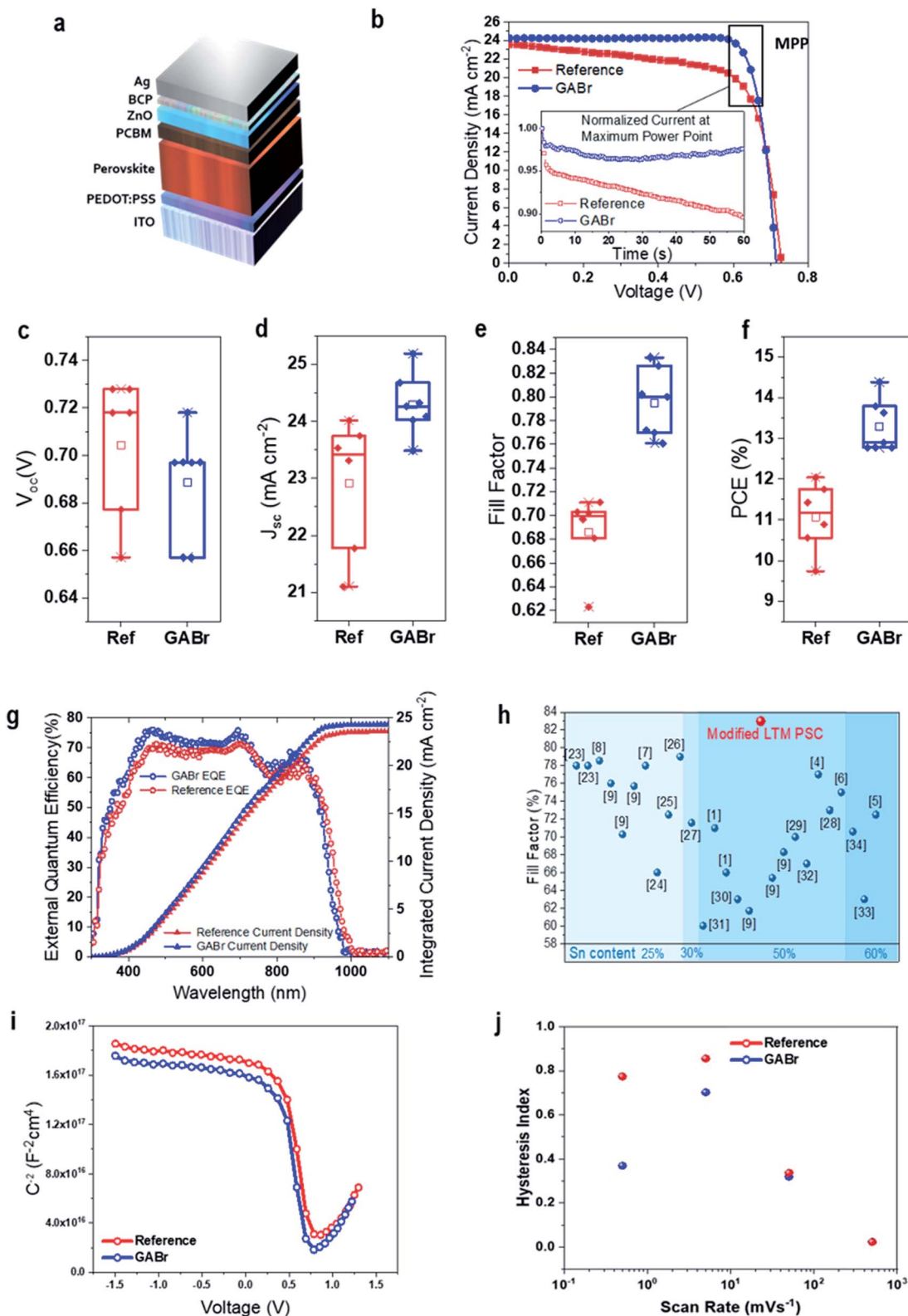


Fig. 5 Photovoltaic device performance comparison before and after surface treatment. (a) Schematic representation of the PV device stack (not drawn to scale). (b) J - V characteristics of the champion and GABr treated devices with the maximum power point shown as MPP (inset: PCE tracking at the MPP). Box plots for (c) V_{oc} , (d) J_{sc} , (e) FF and (f) PCE comparison of the PV devices. (g) EQE profiles of the devices with the integrated current densities. (h) Comparison of literature FF values for different Pb-Sn mixed PV devices (references given within brackets) with that in the current work (indicated by a red sphere). (i) $1/C^2$ vs. voltage measurements for Mott-Schottky analysis and (j) the hysteresis index for the reference and GABr treated LTM perovskite absorbers.

Table 1 Photovoltaic device performance parameters. The principle photovoltaic device parameters for reference and GABr treated LTM perovskite PVs. The average values are presented on results from 6–7 devices. The devices were tested using an aperture with an area of 0.43 cm² with a Pb : Sn ratio of 0.5 : 0.5 in the inverted device configuration

Device parameters	Reference LTM		GABr surface treated LTM	
	Average	Champion device	Average	Champion device
V_{oc} (V)	0.70 ± 0.03	0.73	0.69 ± 0.02	0.72
J_{sc} (mA cm ⁻²)	22.9 ± 1.2	23.5	24.3 ± 0.5	24.3
FF (%)	68.6 ± 3.3	70.3	79.5 ± 2.8	82.6
PCE (%)	11.1 ± 0.9	12.0	13.3 ± 0.7	14.4

place only through a 1st order process (*i.e.* Shockley–Read–Hall mechanism) with very low injection from the contacts (*i.e.* $n = 1$), an FF₀ limit of ~88% is estimated. To account for the ~5% FF deficit, we proceeded to estimate n based on the illumination intensity dependence of V_{oc} as described by³⁶

$$V_{oc} = \frac{nkT}{q} \ln\left(\frac{J_{ph}}{J_s} + 1\right) \quad (6)$$

which under the conditions where $\frac{J_{ph}}{J_s} \gg 1$ and J_{ph} varies linearly with illumination intensity L can be written as

$$V_{oc} = \frac{nkT}{q} \ln(L) + C \quad (7)$$

where C is a temperature dependent value. Based on illumination intensity dependent measurements (Fig. 6b), an ideality factor of ~1.2 is estimated for the GABr treated samples which places an upper limit of ~86% for FF₀ (Fig. 6b). This 3% loss in FF can be attributed to a number of factors such as 2nd order recombination and resistive losses in the contact layout used. We note that further gains can be achieved especially through further optimization of the active layer, charge selective layers³⁷ and engineering for the series resistance losses for the transparent contact.

Energy level alignment and proposed mechanism for enhanced FF

Previously, based on OPTP measurements, we identified that the GABr treatment does not have a noticeable impact on the interband recombination times, indicating that the enhanced

fill factors are most likely due to the alignment of energy levels between the perovskite and the hole and electron transport layers (HTL and ETL), which can result in improved carrier extraction. For this purpose, we carried out ultraviolet photoelectron spectroscopy (UPS) analysis to identify the impact of GABr treatment on the surface electronic properties of the LTM perovskite absorbers (Fig. 7).

We observe shifting of the valence (VB) and conduction band (CB) to deeper energy values following the GABr treatment while the Fermi level E_f is observed to shift closer to the CB edge (Fig. 7d). Previously, based on ToF-SIMS measurements, we have identified the back (*i.e.* GABr treated) surface and the front surface to be compositionally similar. In this scenario, we can assume that both the HTL and the ETL form junctions with a perovskite layer whose electronic properties are akin to those measured for the GABr treated LTM perovskite films. Considering the scenario for hole extraction, the shallower E_f of the GABr treated LTM results in the formation of a more favourable field for hole extraction at the PEDOT:PSS/GABr treated LTM perovskite interface in comparison to the untreated LTM perovskite (Fig. 7e). It is noted that the relative shift of the work function of PEDOT:PSS can also be unfavourable for device performance as the selective carrier extraction can be lost in some instances. However, the shift that is anticipated to take place on this occasion is not detrimental to the device performance as evident from the device characteristics discussed previously. Similarly, for electrons, the deeper E_f for the untreated LTM perovskite results in the formation of a higher barrier for charge transfer from the LTM perovskite absorber to

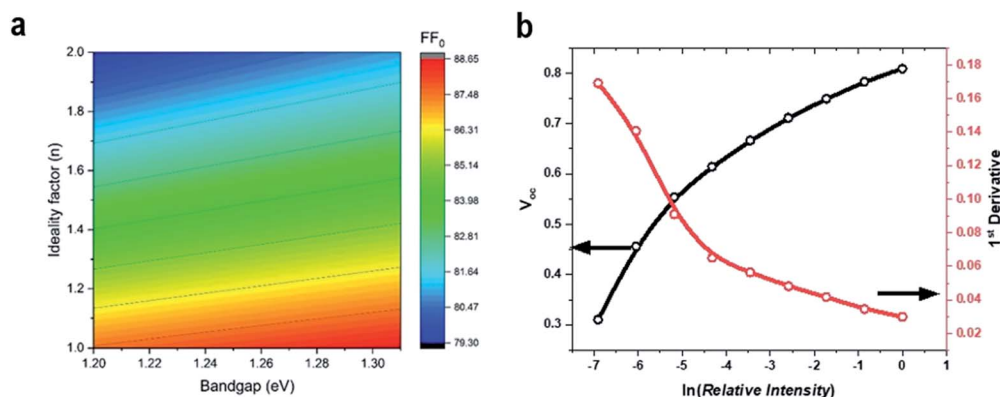


Fig. 6 (a) FF₀ estimation. Estimated maximum fill factors (FF₀) based on varying semiconductor absorber layer bandgap and varying ideality factors (n). (b) Fits for the estimation of n for the reference and GABr treated devices based on illumination intensity dependence of the V_{oc} .

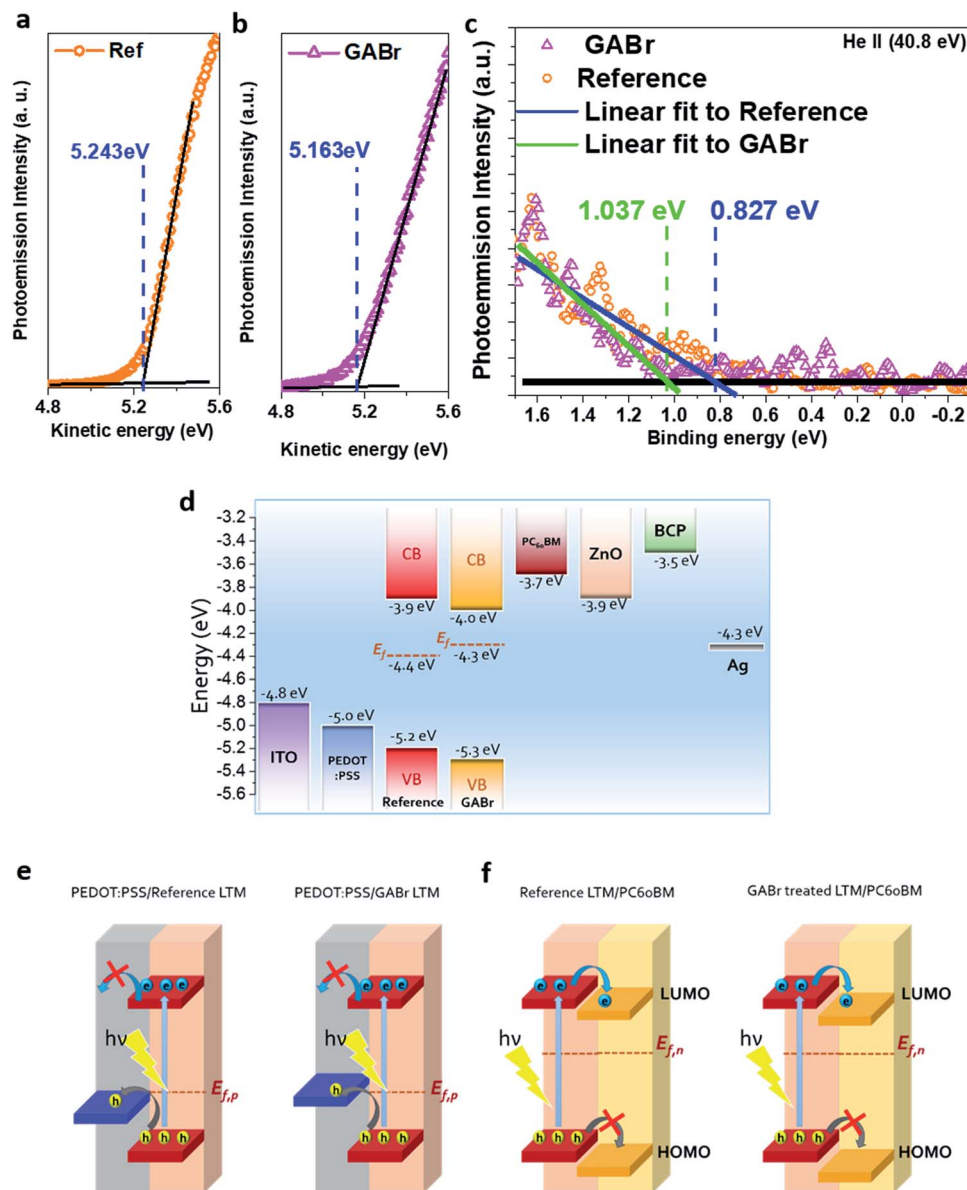


Fig. 7 Work function and valence band position analysis of the perovskite thin films. Low kinetic energy cut-off of (a) reference and (b) GABr treated LTM layers. (c) Valence band spectra (band onsets shown here) for the aforementioned samples. (d) Schematic diagrams indicating the band positions for the perovskite layers as calculated from UPS spectra, along with the band positions of the layers in the device stack. Schematic diagrams of (e) the alignment of the PEDOT:PSS Fermi level with the quasi Fermi level for holes ($E_{f,p}$) of the untreated (left) and GABr treated LTM perovskite layers. The shallower E_f in the GABr treated LTM perovskite absorber results in more efficient extraction of holes at the anode in comparison to the untreated LTM perovskite. Similarly, (f) shallower E_f in the GABr treated LTM perovskite results in a lower barrier for electron extraction which is increased in the absence of the GABr treatment.

the fullerene (Fig. 7f). On the other hand, the incorporation of Br^- into a low bandgap $\text{Cs}_{0.05}\text{FA}_{0.79}\text{MA}_{0.16}\text{Pb}_{0.5}\text{Sn}_{0.5}\text{I}_3$ perovskite absorber results in the formation of a more electron doped perovskite layer. The resulting shifts in the conduction band, valence band and Fermi level energies reduce the barrier for both hole and electron transfer from the LTM perovskite absorber to the anode and cathode contacts in comparison to the untreated $\text{Cs}_{0.05}\text{FA}_{0.79}\text{MA}_{0.16}\text{Pb}_{0.5}\text{Sn}_{0.5}\text{I}_3$ perovskite absorber, which enables fill factors exceeding 80% to be achieved. The GABr treatment demonstrated in this work opens a new route to increase the efficiencies of single junction Sn-

based perovskite PVs towards the Shockley–Queisser limit and is also expected to provide a route to significantly improve the efficiencies of all-perovskite multi-junction cells.

Experimental section

Materials and solvents

Formamidinium iodide (FAI, $\geq 98\%$), methylammonium iodide (MAI, $\geq 98\%$), cesium iodide (CsI_2), tin fluoride (SnF_2 , 99%), tin iodide (SnI_2 , 99.99%), guanidinium bromide (GABr, $\geq 98\%$), aluminum-doped zinc oxide (Al-ZnO nanoparticle ink, 2.5 wt%),

and 1,2,9-dimethyl-4,7-diphenyl-1,10-phenanthroline (BCP; sublimed grade, Sigma Aldrich, 99.99% purity) were purchased from Sigma Aldrich (UK). Lead(II) iodide (PbI_2 , 99.99%) was purchased from Tokyo Chemical Industry Co., Ltd. (TCI, Japan), and [6,6]-phenyl-C61-butyric acid methyl ester (PC_{60}BM) was purchased from Solenne B.V. and poly(3,4-ethylenedioxythiophene) (PEDOT:PSS; Heraeus Clevis P VP AI 4083) was purchased from Ossila. Solvents dimethyl sulfoxide (DMSO, anhydrous, $\geq 99.9\%$), *N,N*-dimethylformamide (DMF, anhydrous, 99.8%), methanol (HPLC grade, $\geq 99.9\%$), chlorobenzene (anhydrous, 99.8%), 2-propanol (anhydrous, 99.5%) and toluene (anhydrous, 99.8%) were purchased from Sigma Aldrich (UK).

Solution preparation

Perovskite precursor solution. PbI_2 , FAI, and MAI powders were dissolved in a glass vial with a DMF : DMSO 4 : 1 (v/v) solvent mixture and stirred for at least 12 h in a N_2 filled glovebox (MBraun MB20G). SnF_2 and SnI_2 powders were added to this solution and stirred for at least 1 h. The final concentrations of the dissolved salts were 0.65 M (0.05 M PbI_2 in excess), 1 M, 0.2 M, 0.12 M and 0.6 M, respectively. To this, 42 μl of CsI (390 mg ml^{-1} in DMSO) was added and stirred for another 30 min.

Hole transport materials. PEDOT:PSS was diluted 1 : 2 (v/v) in methanol under ambient conditions.

Electron transport materials. 20 mg of PC_{60}BM powder was dissolved in 1 ml of chlorobenzene in a N_2 filled glovebox.

Electron transport materials. Al doped ZnO nanoparticle ink was diluted 1 : 1 (v/v) in 2-propanol and sonicated in an ultrasonic bath for 5 min at 100 W.

Guanidinium bromide treatment solution. 5 mg of GABr was dissolved in 1 ml of 2-propanol overnight.

Device fabrication

PV devices were fabricated on 15 mm \times 15 mm \times 0.7 mm ITO (indium tin oxide; $\text{In}_2\text{O}_3:\text{Sn}$) coated glass substrates (Luminescence Technology Corporation, 15 Ω per square), which were first run through a cleaning cycle of sequential sonication in acetone, 2-propanol and methanol for 5 min each, in an ultrasonic bath at 100 W, and subsequently dried under N_2 gas and exposed to O_2 plasma for 5 min. The hole transporting layer was then spin coated on the ITO substrates at 3000 rpm for 25 s under ambient conditions and annealed at 150 $^\circ\text{C}$ for 10 min on a hot plate. The coated substrates were then transferred into a N_2 filled glovebox where each substrate was spin coated with 30 μl of perovskite absorber layer sequentially at 1000 rpm for 8 s, and 6000 rpm for 37 s. 75 μl of toluene anti-solvent was dropped 5 s prior to the end of the spinning cycle, and the coated substrates were annealed at 120 $^\circ\text{C}$ for 20 min inside the glovebox. The samples were taken out of the hot plate and left to cool down for 5 min, before spin coating with 100 μl toluene at 6000 rpm for 30 s to remove any oxidized Sn species, followed by annealing at 120 $^\circ\text{C}$ for 5 min. For the surface treated devices, the samples were then coated with 50 μl of the GABr solution at 5000 rpm for 30 s and annealed at 120 $^\circ\text{C}$ for 10 min, followed by

coating with 50 μl of 2-propanol at 5000 rpm for 30 s. All samples were then cooled to room temperature, and each was spin coated with a 30 μl PC_{60}BM electron transport layer, at 1000 rpm for 35 s. As the next electron transport layer, Al doped ZnO nanoparticle solution was then spin coated at 5000 rpm for 30 s. Finally, the devices were loaded on a shadow mask and a 7 nm thick BCP layer and a 120 nm thick silver cathode were thermally evaporated under a base pressure of $<3 \times 10^{-6}$ mbar at a rate of 0.5 \AA s^{-1} .

Device characterization

Current–voltage characteristics. The current–voltage characteristics of the devices (active area = 0.68 cm^2) were studied in a N_2 atmosphere, under an AM 1.5G 1 sun solar spectrum generated by an ABET 10500 solar simulator (class AAB) with a 150 W Xe arc lamp, calibrated to 100 mW cm^{-2} with a reference Si cell (Newport, PVM 165). PV devices were connected directly to a Keithley 2400 source measure unit (SMU) as the external load. The devices were illuminated through an aperture mask of 0.433 cm^2 open area.

External quantum efficiency (EQE) measurements. The EQE characteristics of the test devices were measured using a Bentham PVE300 system under ambient conditions. Devices were biased under short circuit conditions and EQE was measured using a dual quartz/halogen light source with illumination wavelengths in the range of 300–1100 nm.

Capacitance–voltage, and illumination intensity dependence measurements. Capacitance–voltage and illumination intensity measurements were carried out using Fluxim's Paios all-in-one test platform. Devices were fabricated using the same methodology described for photovoltaic device characterisation. The pixel area was set to 5.6 mm^2 in order to minimise capacitive effects that can influence device characteristics.

Scanning electron microscopy imaging. Samples for SEM were prepared on cleaned and O_2 plasma treated silicon substrates or ITO coated glass substrates by spin coating the LTM layer (with and without surface treatments) following the same procedure as in device fabrication. Prior to SEM measurements, electrical contacts were made using conductive silver ink between the metal SEM stub and the perovskite thin layer. The samples were investigated with an FEI Quanta 200F Environmental SEM setup under a vacuum of $<10^{-5}$ mbar.

To investigate the cross sections, the samples were milled using an FEI Nova Nanolab Focused Ion Beam (FIB) system, and mounted at an angle of 52 $^\circ$ before imaging. Prior to milling, the area of interest of the perovskite layer was enclosed by a protective Pt coating by EBID (electron beam induced deposition) at 5 keV and ~ 1 nA, followed by Pt-IBID (ion beam induced deposition) at 30 keV and 0.4 nA, under a vacuum of $\sim 5 \times 10^{-6}$ mbar. The cross section was made using a Ga^+ ion beam at 30 keV and 0.4 nA. Subsequently, a cleaning cross section step was carried out at 5 keV and a lower current.

Energy dispersive X-ray (EDX) spectroscopy. Samples for SEM were prepared by coating the LTM layer on cleaned silicon substrates. The EDX analysis was carried out on the samples through an x-act Oxford Instruments EDX detector coupled with

a Zeiss Supra 40 SEM setup. The images were analyzed using INCA software from Oxford Instruments. Cross-sectional EDX was performed with a 52° rotation of the sample.

X-ray diffraction (XRD) measurements. For thin film XRD measurements, LTM perovskites were coated on ITO coated glass substrates. XRD spectra were obtained based on the $\text{CuK}\alpha 1$ (1.54060 Å) emission from a Rigaku Mini Flex 600 system.

Ultraviolet-visible (UV-Vis) spectroscopy. The UV-Vis absorption of the LTM thin films was measured using a Varian Cary 5000 UV-Vis-NIR spectrometer fitted with a transmission accessory. The LTM samples were prepared on glass substrates.

X-ray photoelectron spectroscopy (XPS). XPS analyses were performed on a Thermo Fisher Scientific Instruments (East Grinstead, UK) K-Alpha+ spectrometer. XPS spectra were acquired using a monochromated Al $\text{K}\alpha$ X-ray source ($h\nu = 1486.6$ eV). An X-ray spot of ~ 400 μm radius was employed. Survey spectra were acquired employing a pass energy of 200 eV. High resolution, core level spectra for all elements were acquired with a pass energy of 50 eV. All spectra were charge referenced against the C1s peak at 285 eV to correct for charging effects during acquisition. Quantitative surface chemical analyses were calculated from the high resolution, core level spectra following the removal of a non-linear (Shirley) background. The manufacturers' Avantage software was used and it incorporates the appropriate sensitivity factors and corrects for the electron energy analyser transmission function.

Ultraviolet photoelectron spectroscopy (UPS). UPS measurements were carried out at room temperature using a custom setup equipped with a helium discharge lamp and SCIENTA RS4000 photoelectron analyser. The valence-band photoemission spectra were obtained at a pass energy of 10 eV using monochromated He II radiation (40.8 eV). The work function was evaluated from the secondary electron cut-off measured at a pass energy of 2 eV with He I α radiation (21.22 eV) on the sample biased at -5 V. The Fermi energy was evaluated from the Fermi edge of an Au(111) single crystal.

Surface analysis by ToF-SIMS. ToF-SIMS analyses were carried out on an ION-TOF GmbH (Münster, Germany) TOF-SIMS 5 system. The instrument is equipped with a reflectron type analyser and microchannel plate detector. A Bi liquid metal ion source (LMIS) was employed for mass data acquisition. Mass data were acquired using the Bi^{3+} cluster ion. Mass data acquisition was performed by raster scanning over a 100×100 μm^2 area. A 25 keV Bi^{3+} primary ion beam delivering a current of 0.18 pA was used. A cycle time of 100 μs was employed for mass data acquisition. A Cs ion source was employed as the sputter/etch tool. The area analysed by the LMIS was at the centre of the sputter/etch crater formed using the rastered Cs^+ beam. A 3 kV Cs^+ primary ion beam was employed. The Cs^+ sputter/etch area was 400×400 μm^2 . A sputter/etch interval of 1 s was used for all of the depth profile studies described here. The depth profiling analyses were performed in the 'non-interlaced' mode, that is, repeat cycles of mass data acquisition by the Bi LMIS and 1 s sputter/etch by the Cs source, followed by 1 s charge compensation using a low energy electron flood gun were employed.

Terahertz spectroscopy. An optical pump terahertz probe spectrometer based on an ultrafast Ti:sapphire amplifier (Newport Spectra Physics Spitfire Ace, 13 mJ, 1 kHz, 40 fs) was used. Pump pulses with 50 fs duration were generated using a TOPAS Prime optical parametric amplifier pumped by a 3 mJ amplifier beam. Optical rectification in GaP was used for the generation of the terahertz probe which was then detected by electro-optic sampling in ZnTe, using a balanced photodiode scheme and a Pico Technology PicoScope 4262 oscilloscope for data acquisition. A four-pulse scheme, where the terahertz beam and the optical pump are chopped at 500 Hz and 250 Hz (respectively), provided the transmitted terahertz electric field amplitudes E_{off} and E_{on} , with $\Delta E/E = (E_{\text{on}} - E_{\text{off}})/E_{\text{off}}$. The knife-edge method was used to measure the terahertz and optical pump beam diameters resulting in a Gaussian profile with a standard deviation of 300 μm for the terahertz beam and 1.2 mm for the optical pump beam. A gold retroreflector mounted on a motorized stage was used to generate a 3 ns delay line between the terahertz generation and detection beams relative to the fixed optical pump beam.

Steady state photoluminescence spectroscopy. A Horiba Jobin Yvon (HJY) Fluorolog spectrofluorometer was used to obtain the steady state photoluminescence spectra. The samples were illuminated with 475 nm light (bandwidth 29 nm) from a 450 W xenon lamp with a monochromator, at an intensity of approximately 400 W m^{-2} . The photoluminescence was measured with an HJY iHR320 spectrometer coupled to a DSS-IGA020L detector.

Author contributions

I. J. and I. B. conceived the project, fabricated and tested the devices and analyzed the data. M. M., E. B.-C. and J. L. H. conducted P. L. and THz measurements and analyzed the data. I. J., I. B. and S. J. fabricated and tested the devices for IMVS, capacitance-voltage and illumination intensity dependent electrical measurements. Z. W. conducted thin film XRD and strain analysis. W. Z. contributed towards the strain analysis. S. H. conducted XPS measurements and analysis. H. S. & T. P. conducted UPS measurements and analysis. I. J., I. B. and R. S. contributed towards the UPS analysis. M. M. and M. P. conducted SEM and EDX on cross sections. H. T. conducted SEM imaging on films. S. S. directed and supervised the project. I. J. and I. B. wrote the first draft. All authors reviewed and commented on the paper.

Conflicts of interest

There are no conflicts to declare.

Acknowledgements

K. D. G. I. J., R. M. I. B., H. M. T., and S. R. P. S. gratefully acknowledge support from EPSRC *via* research grant EP/R025304/1 and the European Commission H2020 CORNET program (Grant ID: 760949). J. L.-H., M. M. and E. B.-C. acknowledge support *via* EPSRC (Grant ID: EP/N010825/1).

R. M. I. B. acknowledges support from the University of Surrey Overseas Research Scholarship/University Research Scholarship. H. S. acknowledges financial support from the Austrian Science Fund (FWF), project P30431-N36, and the Czech Science Foundation (GACR), project 19-15217S. S. R. P. S. and K. D. G. I. J. also acknowledge Equality Foundation of Hong Kong for financial support for this work.

Notes and references

- G. E. Eperon, T. Leijtens, K. A. Bush, R. Prasanna, T. Green, J. T.-W. Wang, D. P. McMeekin, G. Volonakis, R. L. Milot, R. May, A. Palmstrom, D. J. Slotcavage, R. A. Belisle, J. B. Patel, E. S. Parrott, R. J. Sutton, W. Ma, F. Moghadam, B. Conings, A. Babayigit, H.-G. Boyen, S. Bent, F. Giustino, L. M. Herz, M. B. Johnston, M. D. McGehee and H. J. Snaith, *Science*, 2016, **354**, 861–865.
- M. Saliba, T. Matsui, K. Domanski, J.-Y. Seo, A. Ummadisingu, S. M. Zakeeruddin, J.-P. Correa-Baena, W. R. Tress, A. Abate, A. Hagfeldt and M. Grätzel, *Science*, 2016, **354**, 206–209.
- R. Prasanna, A. Gold-Parker, T. Leijtens, B. Conings, A. Babayigit, H.-G. Boyen, M. F. Toney and M. D. McGehee, *J. Am. Chem. Soc.*, 2017, **139**, 11117–11124.
- G. Kapil, T. S. Ripolles, K. Hamada, Y. Ogomi, T. Bessho, T. Kinoshita, J. Chantana, K. Yoshino, Q. Shen, T. Toyoda, T. Minemoto, T. N. Murakami, H. Segawa and S. Hayase, *Nano Lett.*, 2018, **18**, 3600–3607.
- D. Zhao, Y. Yu, C. Wang, W. Liao, N. Shrestha, C. R. Grice, A. J. Cimaroli, L. Guan, R. J. Ellingson, K. Zhu, X. Zhao, R.-G. Xiong and Y. Yan, *Nat. Energy*, 2017, **2**, 17018.
- J. Tong, Z. Song, D. H. Kim, X. Chen, C. Chen, A. F. Palmstrom, P. F. Ndione, M. O. Reese, S. P. Dunfield, O. G. Reid, J. Liu, F. Zhang, S. P. Harvey, Z. Li, S. T. Christensen, G. Teeter, D. Zhao, M. M. Al-Jassim, M. F. A. M. van Hest, M. C. Beard, S. E. Shaheen, J. J. Berry, Y. Yan and K. Zhu, *Science*, 2019, **364**, 475–479.
- R. Lin, K. Xiao, Z. Qin, Q. Han, C. Zhang, M. Wei, M. I. Saidaminov, Y. Gao, J. Xu, M. Xiao, A. Li, J. Zhu, E. H. Sargent and H. Ta, *Nat. Energy*, 2019, **4**, 864–873.
- T. Leijtens, R. Prasanna, K. A. Bush, G. E. Eperon, J. A. Raiford, A. Gold-Parker, E. J. Wolf, S. A. Swifter, C. C. Boyd, H.-P. Wang, M. F. Toney, S. F. Bent and M. D. McGehee, *Sustainable Energy Fuels*, 2018, **2**, 2450–2459.
- D. Zhao, C. Chen, C. Wang, M. M. Junda, Z. Song, C. R. Grice, Y. Yu, C. Li, B. Subedi, N. J. Podraza, X. Zhao, G. Fang, R.-G. Xiong, K. Zhu and Y. Yan, *Nat. Energy*, 2018, **3**, 1093–1100.
- C. Wang, Z. Song, C. Li, D. Zhao and Y. Yan, *Adv. Funct. Mater.*, 2019, 1808801.
- Z. Yang, A. Rajagopal, S. B. Jo, C.-C. Chueh, S. Williams, C.-C. Huang, J. K. Katahara, H. W. Hillhouse and A. K.-Y. Jen, *Nano Lett.*, 2016, **16**, 7739–7747.
- C. Liu, J. Fan, H. Li, C. Zhang and Y. Mai, *Sci. Rep.*, 2016, **6**, 35705.
- X. Liu, Z. Yang, C.-C. Chueh, A. Rajagopal, S. T. Williams, Y. Sun and A. K.-Y. Jen, *J. Mater. Chem. A*, 2016, **4**, 17939–17945.
- T. S. Sherkar, C. Momblona, L. Gil-Escrig, H. J. Bolink and L. J. A. Koster, *Adv. Energy Mater.*, 2017, **7**, 1602432.
- N. K. Noel, S. D. Stranks, A. Abate, C. Wehrenfennig, S. Guarnera, A.-A. Haghighirad, A. Sadhanala, G. E. Eperon, S. K. Pathak, M. B. Johnston, A. Petrozza, L. M. Herz and H. J. Snaith, *Energy Environ. Sci.*, 2014, **7**, 3061–3068.
- M. Abdi-Jalebi, Z. Andaji-Garmaroudi, S. Cacovich, C. Stavarakas, B. Philippe, J. M. Richter, M. Alsari, E. P. Booker, E. M. Hutter, A. J. Pearson, S. Lilliu, T. J. Savenije, H. Rensmo, G. Divitini, C. Ducati, R. H. Friend and S. D. Stranks, *Nature*, 2018, **555**, 497–501.
- C. Li, Z. Song, D. Zhao, C. Xiao, B. Subedi, N. Shrestha, M. M. Junda, C. Wang, C. -S. Jiang, M. Al-Jassim, R. J. Ellingson, N. J. Podraza, K. Zhu and Y. Yan, *Adv. Energy Mater.*, 2019, **9**, 1803135.
- N. De Marco, H. Zhou, Q. Chen, P. Sun, Z. Liu, L. Meng, E.-P. Yao, Y. Liu, A. Schiffer and Y. Yang, *Nano Lett.*, 2016, **16**, 1009–1016.
- R. M. I. Bandara, K. D. G. I. Jayawardena, S. O. Adeyemo, S. J. Hinder, J. A. Smith, H. M. Thirimanne, N. C. Wong, F. M. Amin, B. G. Freestone, A. J. Parnell, D. G. Lidzey, H. J. Joyce, R. A. Sporea and S. R. P. Silva, *J. Mater. Chem. C*, 2019, **7**, 8389–8397.
- N. D. Pham, V. T. Tiong, D. Yao, W. Martens, A. Guerrero, J. Bisquert and H. Wang, *Nano Energy*, 2017, **41**, 476–487.
- S. Wu, Z. Li, J. Zhang, T. Liu, Z. Zhu and A. K.-Y. Jen, *Chem. Commun.*, 2019, **55**, 4315–4318.
- G. P. Nagabhushana, R. Shivaramaiah and A. Navrotsky, *Proc. Natl. Acad. Sci. U. S. A.*, 2016, **113**, 7717–7721.
- D. J. Kubicki, D. Prochowicz, A. Hofstetter, M. Sasaki, P. Yadav, D. Bi, N. Pellet, J. Lewiński, S. M. Zakeeruddin, M. Grätzel and L. Emsley, *J. Am. Chem. Soc.*, 2018, **140**, 3345–3351.
- W. Zhang, J. Xiong, J. Li and W. A. Daoud, *J. Mater. Chem. A*, 2019, **7**, 9486–9496.
- M. Daub, C. Haber and H. Hillebrecht, *Eur. J. Inorg. Chem.*, 2017, **7**, 1120–1126.
- G. A. MacDonald, M. Yang, S. Berweger, J. P. Killgore, P. Kabos, J. J. Berry, K. Zhu and F. W. DelRio, *Energy Environ. Sci.*, 2016, **9**, 3642–3649.
- Q. Chen, H. Zhou, T.-B. Song, S. Luo, Z. Hong, H.-S. Duan, L. Dou, Y. Liu and Y. Yang, *Nano Lett.*, 2014, **14**, 4158–4163.
- G. Williamson and W. Hall, *Acta Metall.*, 1953, **1**, 22–31.
- I. Robinson and R. Harder, *Nat. Mater.*, 2009, **8**, 291–298.
- N. J. Jeon, J. H. Noh, W. S. Yang, Y. C. Kim, S. Ryu, J. Seo and S. Il Seok, *Nature*, 2015, **517**, 476–480.
- E. S. Parrott, T. Green, R. L. Milot, M. B. Johnston, H. J. Snaith and L. M. Herz, *Adv. Funct. Mater.*, 2018, **28**, 1802803.

- 32 M. Stolterfoht, C. M. Wolff, Y. Amir, A. Paulke, L. Perdigón-Toro, P. Caprioglio and D. Neher, *Energy Environ. Sci.*, 2017, **10**, 1530–1539.
- 33 S. Habisreutinger, N. Noel and H. J. Snaith, *ACS Energy Lett.*, 2018, **3**, 2472–2476.
- 34 H. Tsai, R. Asadpour, J.-C. Blancon, C. C. Stoumpos, O. Durand, J. W. Strzalka, B. Chen, R. Verduzco, P. M. Ajayan, S. Tretiak, J. Even, M. A. Alam, M. G. Kanatzidis, W. Nie and A. D. Mohite, *Science*, 2018, **360**, 67–70.
- 35 M. A. Green, *Solid-State Electron.*, 1981, **24**, 788–789.
- 36 M. Neukom, S. Züfle, S. Jenatsch and B. Ruhstaller, *Sci. Technol. Adv. Mater.*, 2018, **19**, 291–316.
- 37 M. Stolterfoht, P. Caprioglio, C. M. Wolff, J. A. Márquez, J. Nordmann, S. Zhang, D. Rothhardt, U. Hörmann, A. Redinger, L. Kegelman, S. Albrecht, T. Kirchartz, M. Saliba, T. Unold and D. Neher, *Energy Environ. Sci.*, 2019, **12**, 2778–2788.

Supplementary Materials for

Approaching the Shockley-Queisser limit for fill factors in lead-tin mixed perovskite photovoltaics

K.D.G.I. Jayawardena,^{a†} R.M.I. Bandara,^{a†} M. Monti,^b E. Butler-Caddle,^b T. Pichler,^c H. Shiozawa,^{c,d} Z. Wang,^e S. Jenatsch,^f S.J.Hinder,^g M.G.Masteghin,^a M. Patel,^h H.M. Thirimanne,^a W. Zhang,^a R.A. Sporea,^a J. Lloyd-Hughes,^b S.R.P. Silva^{a*}

Correspondence to: s.silva@surrey.ac.uk

XRD analysis

In the range of the measurement, 4 distinctive peaks are seen (**Fig. S4**) at 2θ values of $\sim 14^\circ$, $\sim 20^\circ$, $\sim 24^\circ$ and $\sim 28^\circ$ which were identified to be corresponding to 100, 110, 111, 200 planes respectively, as seen in prior reports for triple cation perovskites.¹ The occurrence of an excess PbI_2 phase is not seen in the LTM films as can be seen by the lack of any peaks at lower 2θ values near the main 100 perovskite peak. The peak positions have shifted to higher 2θ values following the GABr treatment. When fitted with the orthorhombic model;

$$\frac{1}{d_{hkl}^2} = \frac{h^2}{a^2} + \frac{k^2}{b^2} + \frac{l^2}{c^2} \quad (\text{S1})$$

the unit cell parameters can be calculated as, $a = 6.33 \text{ \AA}$, $b = 6.34 \text{ \AA}$, $c = 6.34 \text{ \AA}$ for the reference LTM and $a = 6.32 \text{ \AA}$, $b = 6.29 \text{ \AA}$ and $c = 6.33 \text{ \AA}$ for the GABr treated LTM, clearly showing the contraction of unit cells following the GABr treatment.

Modified Williamson-Hall method for microstrain estimation

Reduction in grain size (Scherrer broadening) and/or non-uniform strain (microstrain) causes a broadening and peak shifts in XRD spectra. It is noted that Scherrer broadening is significant only for grains whose sizes are less than 100 nm which is below that, observed in this work. For crystalline materials, small fluctuations in the lattice spacing as a result of crystal imperfections/structural defects including dislocations, vacancies, stacking faults, interstitials, twinning and grain boundaries²⁻⁴ can result in microstrain. By considering Bragg's law⁵:

$$n\lambda = 2d\sin\theta \quad (\text{S2})$$

where n is an integer, λ is the wavelength of the X-ray energy used, d represents the lattice parameter and θ represents the diffraction angle, it is evident that small fluctuations in d results in small fluctuations, or broadening, in θ . For this work, the extent of microstrain in the LTM perovskite films studied in this work were evaluated by analyzing the peak broadening in the diffraction patterns based on the modified Williamson-Hall method^{2,4}. Under experimental conditions, three factors affect the effective d-space broadening (Δd_{obs}) of an XRD peak. This includes the instrument response (Δd_{ins}), the grain size (Δd_{size}) and the microstrain (Δd_e) width

broadening, which contributes towards the Gaussian full width half maximum broadening in the 2 θ scan. These can be de-convoluted from the observed broadening, via,

$$\Delta d_{obs}^2 = \Delta d_{\varepsilon}^2 + \Delta d_{ins}^2 + \Delta d_{size}^2 \quad (S3)$$

In the above, the unit-less microstrain ε is defined as $\varepsilon = (d_e/d)$, where d is the mean d-spacing. As mentioned above, based on the grain sizes observed in this work, the size effect induced peak width broadening can be neglected. Therefore,

$$(\Delta_{obs}^2 - \Delta_{ins}^2)^{1/2} \approx \varepsilon d \quad (S4)$$

As a result, the microstrain, ε , in the crystals can be estimated from the slope of $(\Delta_{obs}^2 - \Delta_{ins}^2)^{1/2}$ vs d . In contrast to the pristine perovskite film, we can clearly observe an increase in microstrain following the GABr treatment which is attributed to the formation of Cs_{0.05}FA_{0.79}MA_{0.16}Pb_{0.5}Sn_{0.5}(I_{0.8}Br_{0.2})₃ perovskite phase at the grain boundaries of Cs_{0.05}FA_{0.79}MA_{0.16}Pb_{0.5}Sn_{0.5}I₃ and on the film surface.

Estimation of bandgap energies

To estimate the bandgap energies of the LTM films, the steady state photoluminescence (PL) spectra of the two films were investigated. Each film was excited at 475 nm from both surfaces as shown in **Fig. S5**. The resulting spectra show a blue-shift in the peak positions following the GABr treatment. In order to determine the bandgap energies of the LTM perovskites, the back excited PL spectra were fitted with Voigt functions, and centre x-values are taken as the E_{BG} .

Estimation of work function

The work functions were measured with He I α (21.22 eV) on the sample biased at -5 V and the valence band spectra were measured at room temperature with He II (40.8 eV).

The work function (Φ_s) was evaluated as:

$$\Phi_s = E_{cutoff} + E_{bias} + \Phi_A \quad (S8)$$

where E_{cutoff} is the low-kinetic energy cutoff (evaluated in **Fig. 7a & b**); Reference 5.243 eV and GABr 5.163 eV), E_{bias} is the bias potential (-5V) and Φ_A is the work function of the analyser (4.135 eV).

Φ_A was evaluated from the Fermi level of Au(111) single crystal. The work functions with respect to the vacuum level (fermi level; E_f) were calculated as -4.4 eV for the reference LTM and -4.3 eV for the GABr treated LTM.

The valence level with respect to the work function was calculated by the onset of the valence band in each sample (**Fig. 7c**). There appears to be an energy offset of the two samples where the GABr treatment has shifted onset to 1.037 eV compared to 0.827 eV for the reference. The valence band positions were hence calculated to be -5.2 eV for the reference sample and -5.3 eV for GABr LTM. The conduction band positions were evaluated by:

$$CB = VB - E_{BG} \quad (S9)$$

where, CB and VB denotes conduction and valence band energies and E_{BG} is the bandgap energy. As calculated conduction band energies are -3.9 eV for reference and -4.0 eV for GABr LTM.

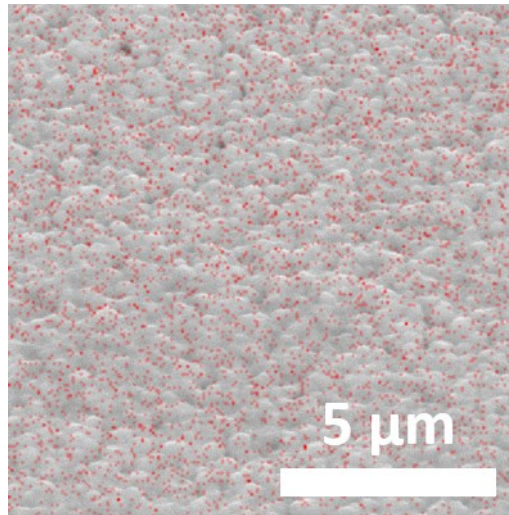


Fig. S1. The EDX mapping of surface of the treated perovskite layer showing homogeneous Br⁻ distribution (indicated by red dots) laid on top of the SEM micrograph of the tested LTM perovskite surface.

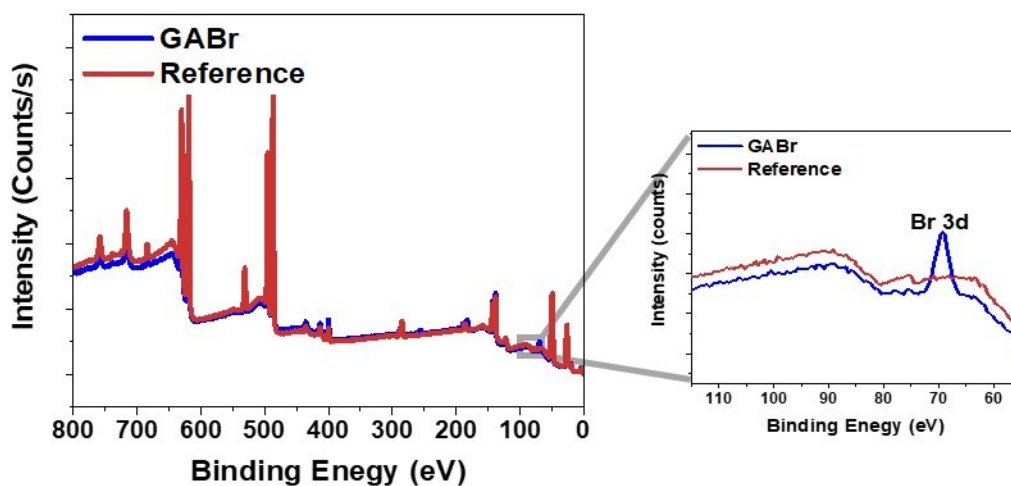


Fig. S2. XPS surface analysis of LTM thin films. The Br 3d peak is clearly visible for the GABr treated sample whereas the reference does not show any such feature. Here, the Br(3d) and I(3d⁵) atomic percentages are 4.37% and 17.07%, resulting in a Br⁻¹ : I⁻¹ ratio of 0.2:0.8. The rest of the spectra are largely seen to be similar in both LTM films showing no major changes in the elemental structure due to the surface treatment.

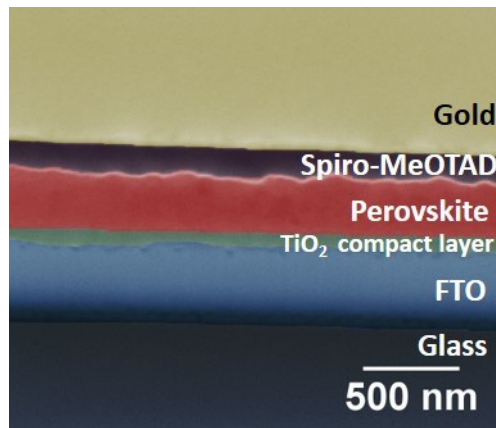


Fig. S3. Cross sectional SEM image of a $\text{Cs}_{0.05}\text{FA}_{0.79}\text{MA}_{0.16}\text{Pb}(\text{I}_{0.85}\text{Br}_{0.15})_3$ film. A bright capping layer on the perovskite layer is observed despite the lack of any additional surface passivation.

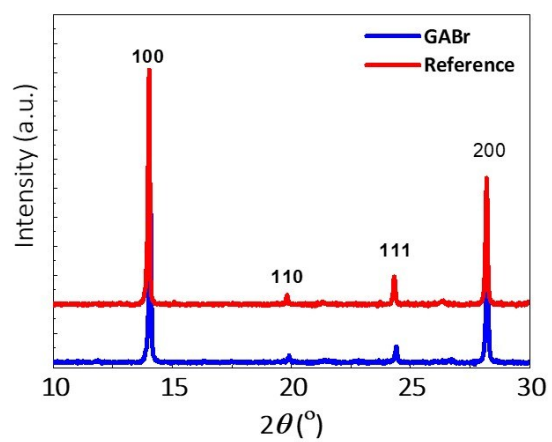


Fig. S4. XRD spectra of LTM perovskite films. Shift in peaks are seen following the GABr treatment to lower lattice spacing.

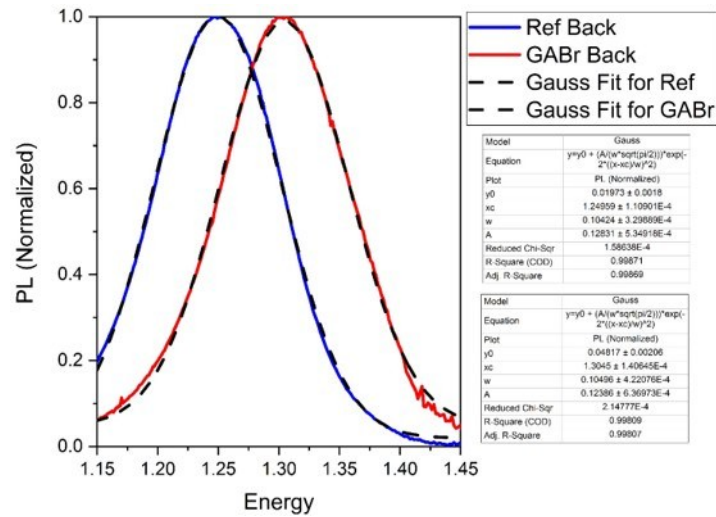


Fig. S5. Fits for determination of bandgap energy (E_{BG}) based on steady state PL spectra obtained from back excitation of the perovskite layer (excitation wavelength = 475 nm). The spectra are fitted with Voigt functions (fittings shown in dotted lines) to obtain the bandgap.

References

- 1 H. Tsai, R. Asadpour, J.-C. Blancon, C.C. Stoumpos, O. Durand, J.W. Strzalka, B. Chen, R. Verduzco, P.M. Ajayan, S. Tretiak, J. Even, M.A. Alam, M.G. Kanatzidis, W. Nie and A.D. Mohite, *Science*, 2018, **360**, 67–70.
- 2 I. Robinson and R. Harder, *Nat. Mater.* 2009, **8**, 291–298.
- 3 A. Pramanick, X.P. Wang, C. Hoffmann, S.O. Diallo, M.R. V. Jørgensen and X.-L. Wang, *Phys. Rev. B.*, 2015, **92**, 174103.
- 4 G. Williamson and W. Hall, *Acta Metall.* 1953, **1**, 22–31.
- 5 M. Birkholz, P.F. Fewster and C. Genzel, *Thin film analysis by X-ray scattering*, Wiley-VCH, 2006.